Computer Simulation of Magnetic Resonance Imaging of Flow of Fluidized Particles

Alireza Bordbar^a, Stefan Benders^b, Wasif Zia^a, Alexander Penn^b, Christopher M. Boyce^{a*}

^a Department of Chemical Engineering, Columbia University, New York, New York, USA

^b Institute of Process Imaging, Hamburg University of Technology, 21073 Hamburg, Germany *Corresponding author, Email: cmb2302@columbia.edu

Abstract

Rapid magnetic resonance imaging (MRI) and velocimetry (MRV) are non-invasive measurement techniques in 3D opaque systems with ~10 ms temporal resolution, enabling new opportunities to challenge the accuracy of computational models of flow. Comparisons between rapid MRI/MRV and computer simulations are limited by: (i) artifacts in rapid MRI techniques and (ii) non-trivial aspects of post-processing of computer simulation data to best match the measurement techniques. Here, we address these issues by starting with data from computer flow simulations of fluidized particles and feeding the data to a physics-based simulation of MRV measurements which captures potential artifacts introduced by the measurement techniques. Flow simulation data is then post-processed in various ways, demonstrating that (1) velocity and particle position data must be taken from flow simulations at different points in time to match MRV measurements and (2) imaging must be faster than flow fluctuation for MRV to produce effectively instantaneous velocity fields.

1 Introduction

Magnetic resonance imaging (MRI) and velocimetry (MRV) are well-established methods of measuring flow in systems relevant to medicine and industry. MRI and MRV enable researchers to non-invasively examine the dynamics within optically opaque systems without the need for tracer particles that are used in typical experimental procedures such as confocal microscopy and Particle Imaging Velocimetry (PIV) ¹. For instance, monitoring packed bed reactors in chemical industry with invasive techniques can only give overall properties such as pressure drop, liquid holdup, wetting efficiency and integral flow rates, while MRI can reveal inhomogeneity of the packing structure responsible for local variations of fluid velocities, holdup, and wetting ². Therefore, in many circumstances, MR-based methods have an advantage over other flow measurement techniques employed in science and engineering. Resonance of nuclear spins of materials within a magnetic field is the phenomenon that forms the basis of nuclear magnetic resonance (NMR). In MRI, the spatial positions of the spins are resolved by applying magnetic field gradients to make the resonant frequency of nuclei depend on their spatial location, leading to "spin-density" images that depict the amount of NMR signal from each location in an image. In MRV, dedicated pulse sequences are employed to additionally determine the displacement of the spins. Phase contrast velocimetry (PCV) is a technique in MRV that enables encoding flow velocities in the x-, y- and z-directions based on the phase of NMR signal produced after applying bipolar pulsed field gradients ³. PCV can be combined with imaging gradients to produce a spatially resolved image of the velocity field in a flow system. Until recently, MRV was limited by temporal resolution to only measure a highly time-averaged velocity in a system 4. Much effort has been dedicated to improve the accuracy and temporal resolution of MRV techniques to measure flow systems with unsteady flow behavior on a temporally resolved level.

Computer simulations which capture the physics of nuclear spin dynamics to model how MR would measure spin density or flow in a sample present an opportunity to evaluate the accuracy of MRI measurements. Ultimately, such insights have the potential to be used to improve accuracy and resolution of MR measurement techniques based on simulations which are inexpensive as compared to conducting MR experiments. MRI simulations can capture the effects of the following aspects on images ⁵ and flow measurements ^{6,7}: (1) the "pulse sequence" of radiofrequency pulses and magnetic field gradients used ^{8–10}, (2) sample NMR properties ¹¹, (3) magnet and radiofrequency coil hardware ¹², (4) sampling and reconstruction algorithm choice ¹³ and (5) background noise ¹⁴. As such, simulations can reveal the difference between the effects arising from MRI physics and those caused by hardware imperfections, and hence, help researchers to optimize the available pulse sequences [3]. MRI simulations can help in designing novel pulse sequences ¹⁵ and reconstruction algorithms ¹³ for certain applications. Lastly, MRI simulations facilitate interpretation and analysis of experimental data through comparison ¹⁶.

Only a handful of studies have simulated MRV to assess the level of accuracy of MRV measurement techniques ^{6,17,18}. These studies have input flow data produced by computational fluid dynamics (CFD) simulations into MRV simulations to produce simulated MRV

measurements of velocity (**Fig. 1**). These studies then compared the input CFD velocity data to the output simulated MRV velocity data to assess the accuracy of MRV measurements ¹⁹. One study has used the software JEMRIS ¹⁶ to conduct MRV simulations on steady flows in a cerebral venous network using CFD ⁶. Another study conducted temporally averaged MRV simulations on granular particle flow simulation data to assess the accuracy of comparing different temporal averaging techniques for flow data with the temporal averaging conducted in MRV ²⁰. Recently, MRV techniques have been combined with rapid imaging pulse sequences to achieve temporally-resolved measurements of granular flows in highly unsteady flow units known as fluidized beds ^{21–24}. While these rapid MRV techniques are promising for characterizing a number of complex flows, potential inaccuracies to MRV introduced by the rapid imaging techniques and fast flow dynamics are difficult to assess. We are unaware of prior MRV simulation studies which have tested rapid MRV pulse sequences for high temporal resolution applied to unsteady flows to characterize the accuracy of these MRV measurement techniques.

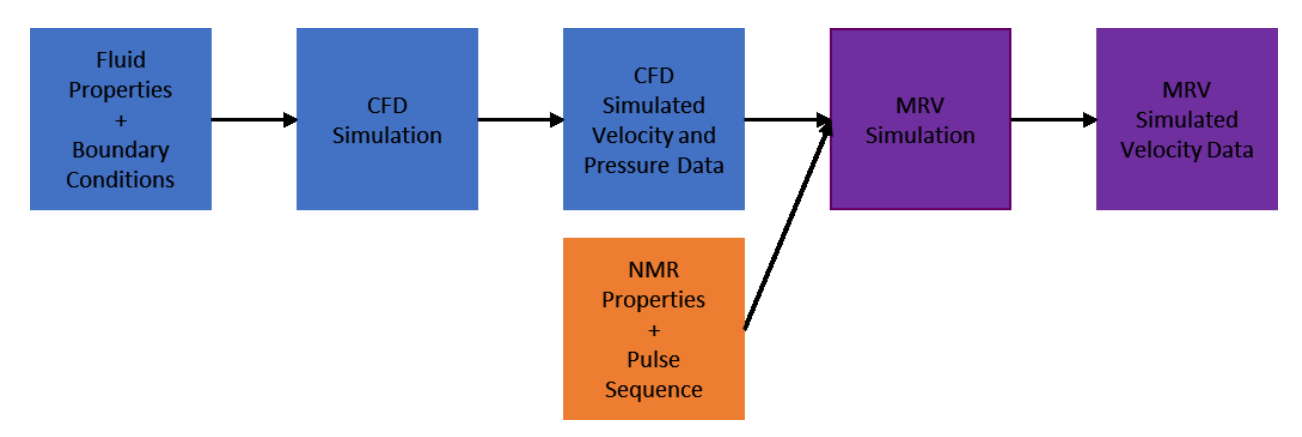


Fig. 1 Schematic of the use of CFD and MRV simulations to assess the accuracy of MRV techniques to measure flow in specific flow systems.

This study seeks to utilize CFD-Discrete Element Method (CFD-DEM) simulations to produce particle flow data for both steady and unsteady flows which then can be fed into MRV simulations to assess the accuracy of MRV techniques in measuring various flows (**Fig. 1**). MRI and CFD-DEM have both been used extensively to study the complex dynamics of fluidized beds ^{25–29}. Fluidized beds involve granular particles suspended by upward gas flow, creating rapid and complex dynamics in process units used in pharmaceuticals, polymers and clean energy technologies ^{30–32}. Several prior studies have compared CFD-DEM simulation results with MRI experiments to assess the accuracy of CFD-DEM simulations, utilizing time-averaged and time-resolved flow data ^{25,33}. One prior study has utilized CFD-DEM data in MRV simulations with time-averaged flow measurements to study the effect of averaging techniques applied to flow measurements on how they compare with MRV measurements ²⁰. Here, we seek to close the loop on recent studies comparing time-resolved CFD-DEM and MRV data. This is achieved by

incorporating MRV simulations that utilize CFD-DEM data to assess the accuracy of rapid MRV experimental techniques (**Fig. 2**). Further, we seek to gain insights into the best ways to post-process CFD and DEM data to create accurate comparisons with MRI techniques, such that discrepancies between simulations and measurements come from inaccuracies in simulations or measurements, rather than inaccuracies in the post-processing for the comparison.

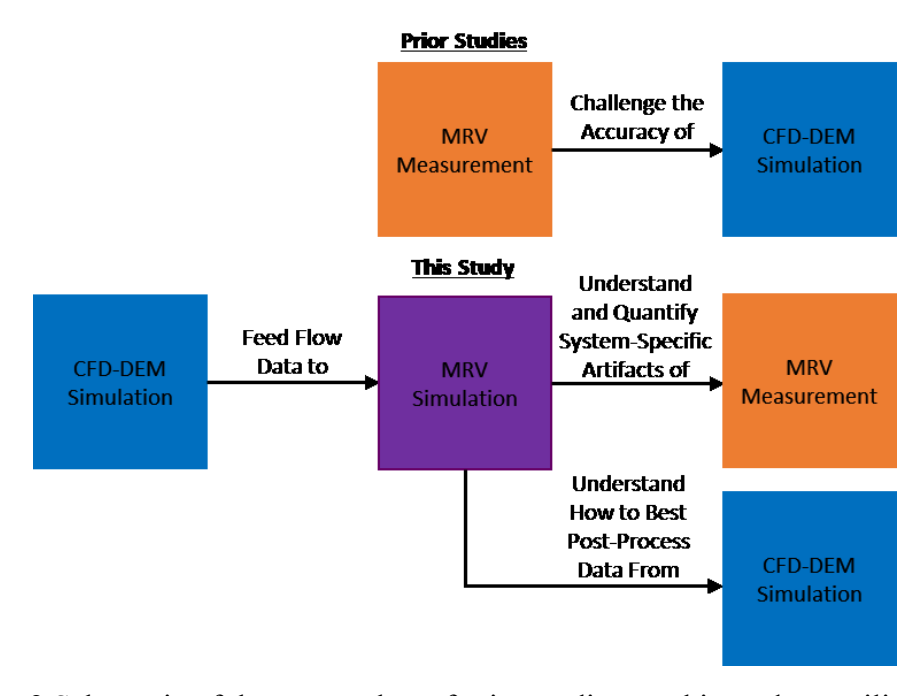


Fig. 2 Schematic of the approaches of prior studies vs. this study to utilize MRV measurements and CFD-DEM simulations to understand the effect of MRV measurement artifacts and identify the best CFD-DEM post-processing methods.

2 Numerical methods

2.1 Flow modeling

The Discrete Element Method (DEM) is a Lagrangian approach that models particle motion through tracking individual particles in space and time. For this purpose, Newton's and Euler's second laws are used for translational and rotational modes of motion, respectively. Cundall and Strack ³⁴ were the first to introduce the DEM method in 1979 utilizing springs and dashpots as well as friction to account for the contact forces which arise between particles. CFD-DEM is the result of coupling this approach with Computational Fluid Dynamics (CFD), which makes it suitable for the simulation of fluid-particle systems. In CFD-DEM, the fluid is treated as a continuum whose motion can be described by volume-averaged Navier-Stokes (NS) equations. The flow field is divided into cells with size larger than the particle, but smaller than the system length scale. The effect of motion of particles on the fluid flow is accounted for by the volume fraction of each phase and the momentum exchange through the drag force ³⁵. On an Eulerian grid

with a cell volume of V_c , the gas-phase volume-averaged NS equations in the presence of the particulate phase are:

$$\frac{\partial(\varepsilon_{g}\rho_{g})}{\partial t} + \nabla \cdot \left(\varepsilon_{g}\rho_{g}\vec{\boldsymbol{u}}_{g}\right) = 0 \tag{1}$$

$$\frac{\partial(\varepsilon_{g}\rho_{g}\vec{\boldsymbol{u}}_{g})}{\partial t} + \nabla \cdot \left(\varepsilon_{g}\rho_{g}\vec{\boldsymbol{u}}_{g}\vec{\boldsymbol{u}}_{g}\right) = -\varepsilon_{g}\nabla p_{g} + \nabla \cdot \bar{\boldsymbol{\tau}}_{g} + \varepsilon_{g}\rho_{g}\vec{\boldsymbol{g}} + \sum_{p=1}^{N_{p}} \beta \frac{V_{p}}{V_{c}}(\vec{\boldsymbol{u}}_{p} - \vec{\boldsymbol{u}}_{g})$$
(2)

where ε_g , ρ_g , p_g , and \vec{u}_g denote the void fraction, density, pressure, and local average velocity of the gas phase, respectively. In Equation (2), the velocity of the solid particle is shown as \vec{u}_p , β is the interphase momentum exchange coefficient, V_p is the volume of each particle, N_p is the total number of particles, and \vec{q} represents the gravitational acceleration.

Forces imposed on the particle include gravity, contact force between particles, and fluid-particle interaction ³⁵. Newton's equations of motion account for the motion of N_p spherical particles with the diameter of d_p and density of ρ_p according to the following:

$$m_p \frac{d\vec{\boldsymbol{u}}_p}{dt} = m_p \vec{\boldsymbol{g}} + \vec{\boldsymbol{F}}_c + \vec{\boldsymbol{F}}_d \tag{3}$$

$$I_p \frac{d\vec{\boldsymbol{\omega}_p}}{dt} = \vec{\boldsymbol{T}_p} \tag{4}$$

where m_p is the particle's mass, \vec{F}_c and \vec{F}_d are the net contact force with other particles and walls and the drag force exerted by the surrounding gas phase, respectively. I_p is the moment of inertia of the particle, $\vec{\omega}_p$ is the particle angular velocity, and \vec{T}_p is the sum of all torques exerted on the particle. Momentum exchange in each fluid flow cell describes the fluid-particle interactions for the fluid phase, while force acting on each individual particle is considered for the fluid-particle drag force for the solid phase.

2.2 Flow simulation setup

In the examined flow systems of this study, spherical particles are moving in a 3D cylindrical container that is 190 mm in diameter at the base and 300 mm in height. The cases that will be studied include two less complex flow situations in which velocities are applied manually to the particles giving them (i) a parabolic velocity profile or (ii) a uniform velocity profile (i.e. plug flow). The two other flow cases come from CFD-DEM simulations of an incipiently fluidized bed into which two side-by-side high-velocity air jets are injected into (iii) 3 mm diameter particles and (iv) 1 mm diameter particles. In cases (iii) and (iv), two ports at the base of the system inject gas rapidly; these ports are 40 mm apart and each have a diameter of 7.95 mm. The minimum fluidization velocity ($U_{\rm mf}$) for the 3 mm particles is 0.7 m/s and 0.25 m/s for the 1 mm particles,

and the bed is incipiently fluidized with a corresponding gas flow rate through the distributor. The gas velocity through the injection ports is set at 40 m/s. **Fig. 3a** shows the CFD-DEM flow setup and the slice that will be ultimately used to extract data from for MRI simulations and CFD-DEM post-processing. **Figs. 3b**-d show cross-sectional views of how the particles attain velocities in different cases. **Fig. 3b** shows the velocities assigned to particles to provide a steady parabolic profile. **Fig. 3c** and **3d** depict how the air jets interact with one another in different manners in fluidized beds with different particles sizes.

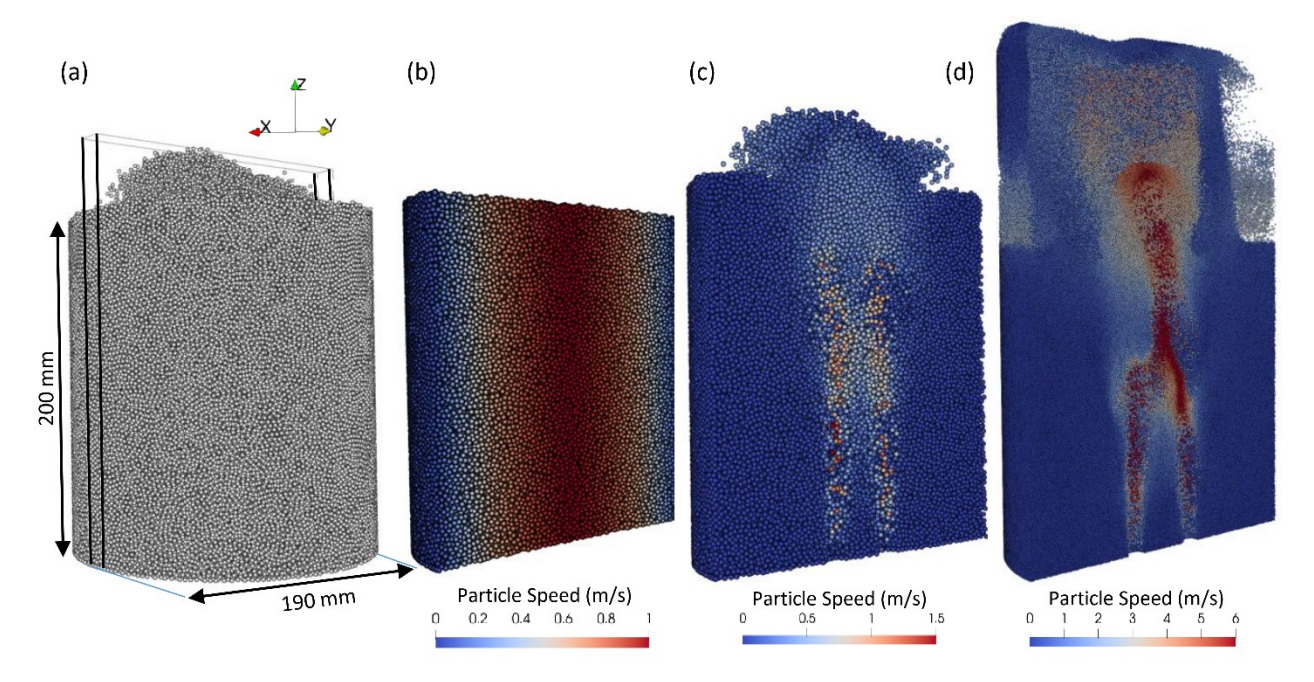


Fig. 3. CFD-DEM simulation setup. (a) The cylindrical bed filled with 3 mm particles and incipiently fluidized with a superficial gas velocity of 0.7 m/s, in addition to injection of two high velocity air jets at 40 m/s. The narrow black box shows the slice used in MRI simulations and to extract data for CFD-DEM post-processing. The same system is used without injection of high velocity air jets to make parabolic and plug flow profiles. (b) cross-sectional view of the system with 3 mm particles and a parabolic flow profile, (c) cross-sectional view of the system with 3 mm particles with $U_{\rm mf} = 0.7$ m/s and air jets' velocities of 40 m/s, (d) cross-sectional view of the system with 1 mm particles with $U_{\rm mf} = 0.25$ m/s and air jets' velocities of 40 m/s.

2.3 Modeling of MRI

JEMRIS (The Jülich Extensible MRI Simulator) software ³⁶ is employed to conduct physics-based simulations of MRV measurements for this study. This package is an extendable MRI simulation framework, written in C++, enabling the users to develop MRI sequences and simulate 3D MRI experiments ³⁷. The key feature of JEMRIS is that, instead of providing predefined MRI sequences and experimental setups, it comes with a number of basic building modules that enable the researchers to construct any new sequences that they desire.

In an MRI simulation, the object to be imaged is divided into equal subvolumes called "isochromats". For convenience, the terms "isochromats" and "spins" will convey the same meaning throughout this text. Taking that into consideration, "isochromats summation" is the simulation method used in JEMRIS, meaning that it sums the magnetization signal generated by each of the spins contained in the system ¹⁹. This is the most popular method used to simulate MRI. The Bloch equations ³⁸ describe quantum MRI physics from a classical physics perspective by giving the temporal evolution of the magnetization vector of the spins, \vec{M} , in the presence of an external magnetic field, \vec{B} , and by taking into account the NMR properties of the sample ³⁹. The NMR properties include the equilibrium magnetization, \vec{M}_0 , the longitudinal relaxation time, T_1 (also known as spin-lattice relaxation time), and the transverse relaxation time, T_2 (also known as spin-spin relaxation time). It is assumed that the isochromats possess uniform physical properties, such as relaxation times, equilibrium magnetization, and magnetic susceptibility ⁴⁰.

The magnetization of each spin is rotated into a transverse plane with respect to the axis of the main magnetic field by application of an RF pulse by an angle determined the duration and strength of the RF pulse. In between the application of RF pulses, the evolution of spin magnetization consists of T_1 recovery, T_2 relaxation, motion, as well as the effect of the applied gradients. A k-space array is formed by summing the contribution of all spins at each time step during "sampling". The ultimate image is generated by Fourier transformation of the k-space data 41 .

The evolution of magnetization of spins within a magnetic field, \vec{B} , can be described by the Bloch equations:

$$\frac{d\vec{M}}{dt} = \gamma \vec{M} \times \vec{B} - \begin{pmatrix} M_{\chi}/T_2 \\ M_{y}/T_2 \\ (M_z - M_0)/T_1 \end{pmatrix}$$
 (5)

where γ is the gyromagnetic ratio. Note that at equilibrium, the net magnetization vector, \vec{M}_0 , points towards the direction of the static magnetic field in z-direction, typically denoted as, \vec{B}_0 . As can be seen, Equation (5) is a set of three equations for each direction of magnetization, $\vec{M} = (M_x, M_y, M_z)$. These equations can be solved to calculate the macroscopic magnetization in a voxel at a certain time ⁴². The macroscopic approach to treat the temporal evolution of spins in a bulk liquid assumes the spins to add up linearly in order to form a net magnetization vector that can be described by Bloch's equations. Using the same argument, in this work we treat the behavior of all spins within one particle as one sum vector which are described by Bloch's equations.

All the MR sequence parameters, including RF pulses and gradients, are accounted for by the magnetic field term \vec{B}^{40} . The expression for this term at time t and position \vec{r} is given by

$$\vec{B}(\vec{r},t) = \left(\vec{G}(t).\vec{r} + \frac{\Delta\omega(\vec{r},t)}{\gamma}\right)\vec{e}_z + \vec{B}_1(\vec{r},t)$$
(6)

where $\vec{G}(t)$ are the gradient fields used to encode position in three spatial directions, $\Delta \omega$ is the off-resonance term, and \vec{B}_1 accounts for the RF field excitation, which is orthogonal to the main field $(\vec{B}_1 \perp \vec{e}_z)^{39,43}$.

MRI simulators usually deal with samples which are static biological tissues. However, the sample in this study is a flow involving traveling spins. Therefore, we are required to determine the trajectory of each individual spin. If we adopt a Lagrangian approach to build the sample file, static tissues and flowing particles will be treated similarly and there is no need to have different solvers for each. In this approach, the position of each spin over time is recorded $(\vec{r} = \vec{r}'(t))$ and fed to the Bloch equation solver to change the field value seen by the particle ⁴⁰:

$$\vec{B}(\vec{r},t) = \left(\vec{G}(t).\vec{r}'(t) + \frac{\Delta\omega(\vec{r},t)}{\gamma}\right)\vec{e}_z + \vec{B}_1(\vec{r},t)$$
(7)

Fortunately, in CFD-DEM simulations, the DEM part is a Lagrangian approach which tracks the particles in space and time. Hence, we can extract the positions of each particle over time and introduce them to JEMRIS as the trajectories of a set of spins. Since JEMRIS default settings address only rigid samples, they allow only one trajectory for all the spins. The ability to import steady-state CFD data into JEMRIS was developed first in 2016 by Ancel et al. ⁴⁰. However, here we are dealing with time-varying DEM data. A Matlab code was therefore written that extracts the position of each particle in the DEM data, and puts them in a certain format, including the activation command for each spin, recording the positions at a certain number of time steps, deactivating it, and then moving to the next spin.

An Echo Planar Imaging (EPI) sequence was implemented within the JEMRIS framework (**Fig.** 4) to compare with existing MRI measurements 24,44 . While recently developed rapid MRI measurements for granular flows employ SENSE and partial-Fourier acceleration 24,45 , a full k-space simulation was performed here. The read and phase prewind were superposed to the velocity encoding gradients, in case velocity was encoded in that x-, y- or z-direction. The repetition time is 2 s, the echo time is 29.43 ms, a slice thickness of 15 mm, a Field-of-View of 195 × 265 mm² with 64 × 64 acquisition points. The Field-of-Flow is set to 6000 mm/s with a $\delta = \Delta$ of 2 ms.

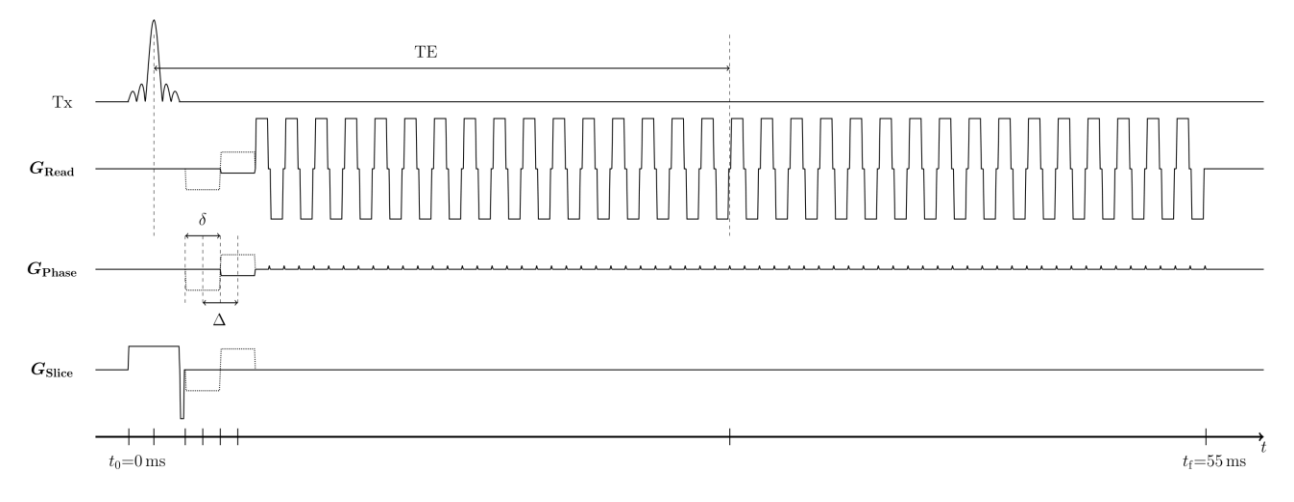


Fig. 4: Pulse sequence diagram of an EPI sequence with 64 lines sampled in k-space. The dotted lines represent the gradients switched if velocity is encoded in the respective gradient direction.

2.4 Other Post-Processing Methods for CFD-DEM Data

For comparison with JEMRIS MRV simulations, the CFD-DEM particle data was post-processed in other manners which would be easier for flow simulation specialists to use to process data for comparison with MRV measurements. Five different methods (Methods a-e) were conducted, as shown schematically in Fig. 5. CFD-DEM data was taken every 0.5 ms, creating a total of 110 frames over the 55 ms of the pulse sequence duration, each frame providing information on the position and velocity of each individual particle. Each particle was mapped into a pixel based on the pixel in which the center of the particle was located. Method a determines particle position and velocity data used to make velocity maps based on averaging 110 frames over the entire duration of the pulse sequence. Method b determines the velocity map based on averaging particle velocity maps over the 11 frames during flow-encoding period. Method c uses the velocity map from a single frame at the center of the flow-encoding period (i.e. the bipolar gradient period). Method e takes the particle velocity data from a single frame at the center of the flow-encoding period and uses the particle position data from a single frame at the center of the imaging period.

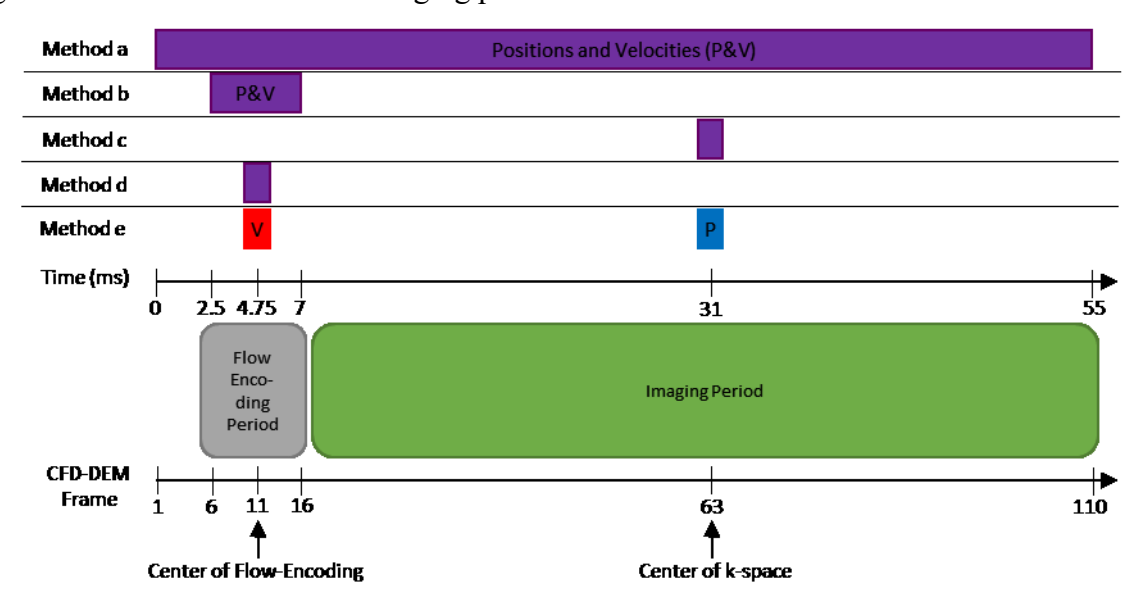


Fig. 5 Schematic of the post-processing methods (*Methods a-e*) other than JEMRIS applied to the particle position and velocity data from CFD-DEM simulations to produce particle velocity maps.

3 Results and discussion

In order to investigate the capability of the developed pulse sequence in JEMRIS to accurately capture the flow phenomena, two simpler cases of flow are studied first. For this purpose, the particles were assigned vertical velocities with parabolic profile shape in one case (Fig. 6, top

row), and uniform flow profile (i.e., plug flow) in the other case (Fig. 6, bottom row). The particles, 3 mm in diameter, reach a maximum vertical velocity of 100 mm/s in both cases. The first column of Fig. 6 shows the results obtained from CFD-DEM simulations on a cross-sectional slice. The local velocities are averaged over a period of 55.22 ms. This is equal to the duration of the implemented MR pulse sequence and makes comparison between JEMRIS and CFD-DEM results possible. In averaging the CFD-DEM results, the velocities are extracted from a 15 mm thick slice, and displayed with a 64×64 resolution, equal to the slice thickness and image resolution used in JEMRIS simulation. The corresponding MRV simulation results are shown in the middle column. The field of view (FoV) and slice position in both CFD-DEM and JEMRIS simulations are as close to one another other as possible. The FoV is 200×200 mm, and the center of the slice is positioned at a height of 150 mm from the inlet. In the third column, the difference between the CFD-DEM and MRI simulations results are depicted. As it can be observed, the difference in both cases is near zero, which demonstrates the accuracy of the MRV simulation platform employed in this study. These results also demonstrate that averaging CFD-DEM data over the full duration of the pulse sequence creates an accurate comparison with the JEMRIS simulations in cases with steady flow.

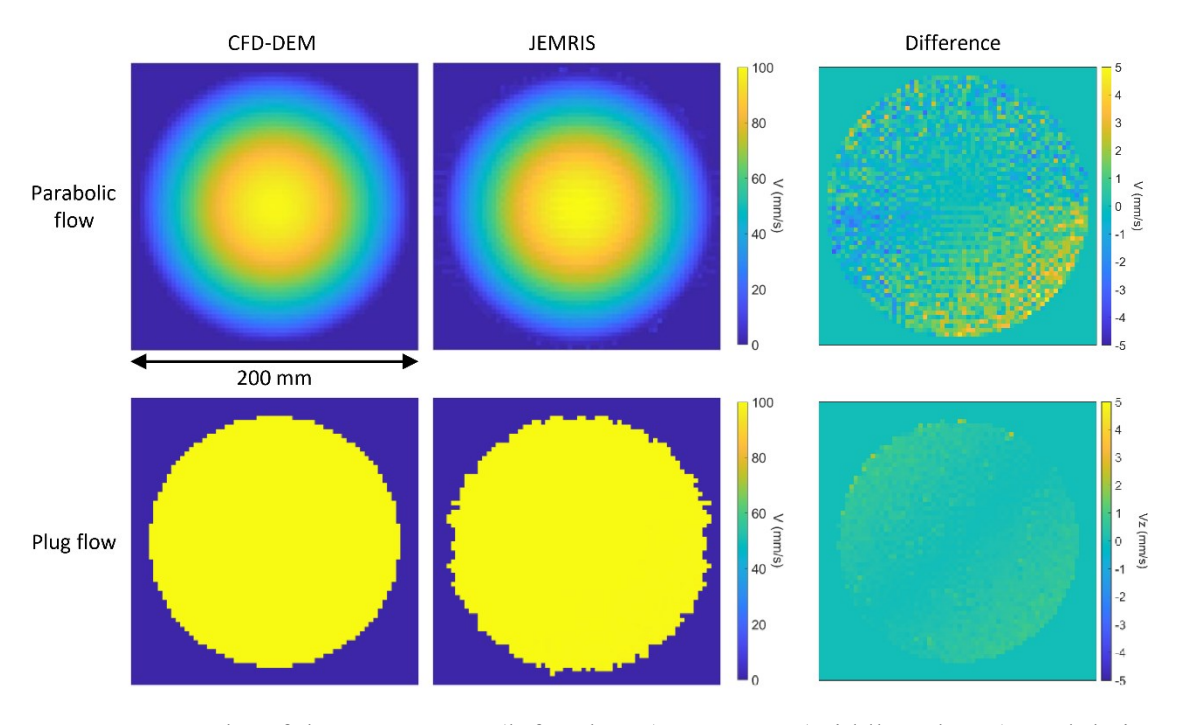


Fig. 6. Results of the CFD-DEM (left column), JEMRIS (middle column), and their difference (right column) for cases of parabolic flow profile (first row) and plug flow profile (second row).

After establishing the functionality of the implemented pulse sequence in JEMRIS, CFD-DEM simulations are conducted for two scenarios of incipiently fluidized beds, along with injection of two high-velocity air jets adjacent to each from the base. The dimensions of the system and the height of the particles filling the system are akin to the cases described above for the plug flow

and parabolic flow simulations. As mentioned earlier, for the case of 3 mm particles, the bed is incipiently fluidized with a gas velocity of 0.7 m/s and the jet velocity through the injection ports is set at 40 m/s. The MRI measurements of this case were previously conducted by Penn et al. ⁴⁴ and time series images of particle concentration from MRI measurements and the CFD-DEM simulations are shown on axial slices in **Fig. 7**. From this figure, it can be observed that CFD-DEM flow simulations can capture the major phenomena of jet interaction and bubble pinch off seen in experiments.

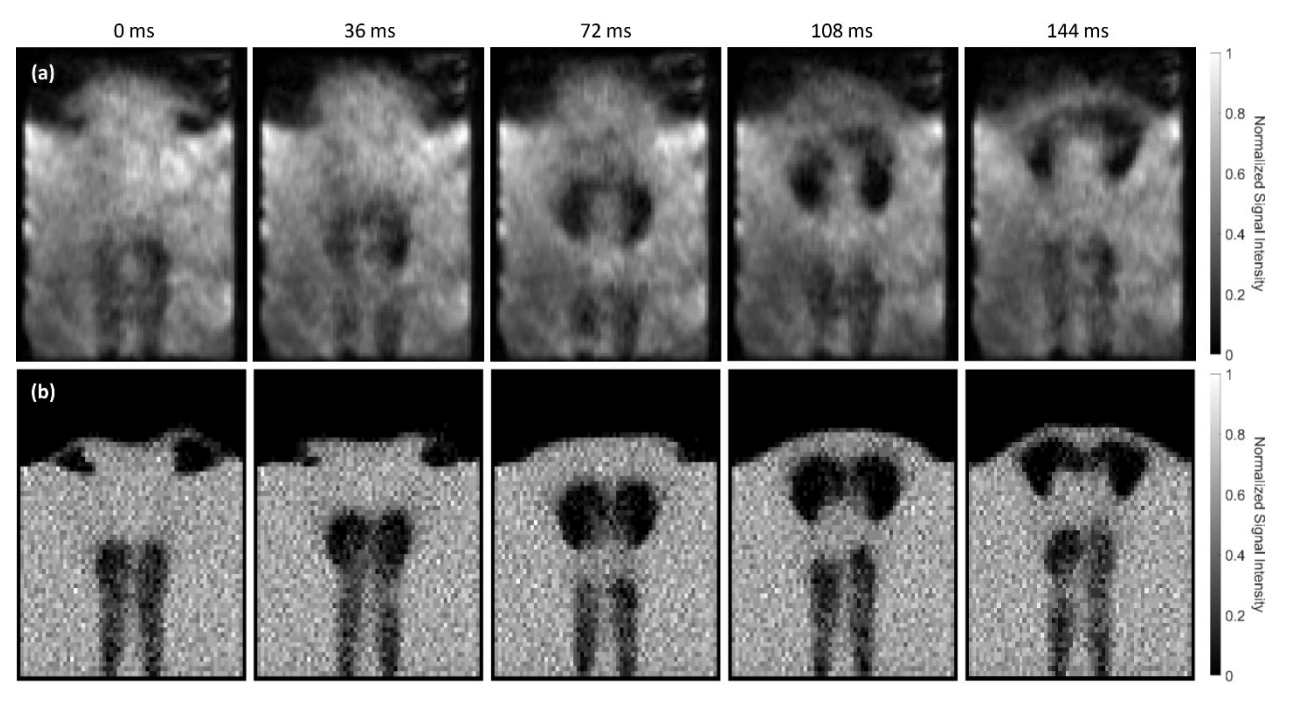


Fig. 7. Time series of signal intensity images of 3-mm particles from (a) prior MRI measurements ⁴⁴ and (b) CFD-DEM simulations. The images represent a central axial slice with a thickness of 10 mm.

The results of the CFD-DEM simulation are then exported to JEMRIS to perform the MRI simulation. **Fig. 8a** shows the signal intensity image obtained on a central axial slice from JEMRIS. The color bar is normalized, such that the maximum signal in the image is shown as 1, and areas without any detected signal are shown as zero. The image represents the signal intensity imaged produced by the full 55-ms-long pulse sequence, and it can be observed that four distinct low-signal regions exist. Two almost identical low-signal areas in the lower half of the figure, near the two injection ports, and another pair around the top surface of the bed, where two bubbles erupt. It was later observed in MRV that these areas show up highly noisy in the velocity plots due to the low signal intensity. Therefore, it was decided to mask the areas in the signal intensity image where the signal magnitude was less than 30% of the maximum signal, and the masked areas were then removed from the subsequent velocity calculations (**Fig. 8b**). Noise in low particle concentration regions was also seen in the prior experimental MRV data, and thus masking was used in the presentation and analysis of the prior data as well ⁴⁴.

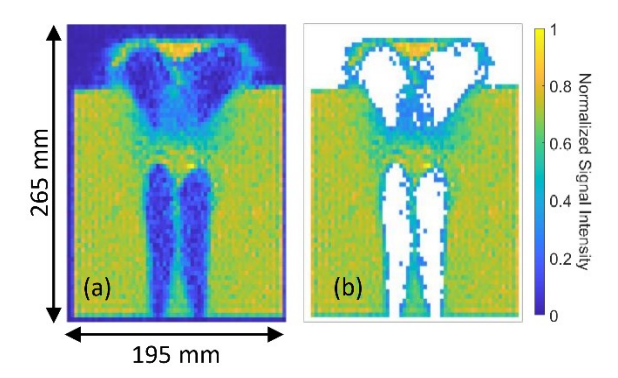


Fig. 8. Signal intensity images taken from a JEMRIS MRI simulation. (a) raw simulation output and (b) masking voxels with less than 30% of the maximum signal intensity with the masked areas removed from calculations.

Fig. 9 shows the vertical component of particle velocity (V_z) on a central slice with a thickness of 15 mm for the fluidized bed of 3 mm particles. The first row of Fig. 9 depicts the JEMRIS results, the second row depicts CFD-DEM data processed with different post-processing techniques and the third row shows the difference between JEMRIS and CFD-DEM with different post-processing techniques. Areas masked due to low particle concentration in either the first or second row of Fig. 9 show up as voided in the corresponding voxel in the difference plot. As can be seen from the third row of Fig. 9, the JEMRIS MRV simulation results are fairly close to the CFD-DEM results in most regions no matter how the CFD-DEM results are processed. However, there are some significant discrepancies in regions with high particle velocity between the jets and the bubbles. Post-processing techniques which give more weight to the velocities of the particles during the imaging portion of the pulse sequence (a and c) provide velocities in the high velocity region which are lower than those seen in the JEMRIS simulation. Post-processing techniques which give more weight to the flow encoding portion of the pulse sequence (b and d) provide velocities which are higher than those seen in the JEMRIS simulation and bubble positions which are lower than those seen in the JEMRIS simulation. Post-processing of the CFD-DEM data such that the particle velocities are taken at the center of the flow encoding yet the particle positions are taken at the center of the imaging gradients match JEMRIS simulation results most closely. The closeness of the match between CFD-DEM and JEMRIS is assessed by the normalized meansquared difference in the velocity measurements:

$$\mu_{MS} = \frac{1}{N} \sum_{i=1}^{N} \left(\frac{J_i - C_i}{C_i} \right)^2 \tag{8}$$

where N is the number of pixels in the FoV, and J_i and C_i denote the vertical velocities in cell i from JEMRIS and CFD-DEM, respectively. The standard deviation of the normalized mean-squared difference was calculated according to:

$$\sigma_{MS} = \sqrt{\frac{1}{N} \sum_{i=1}^{N} \left[\left(\frac{J_i - C_i}{C_i} \right)^2 - \mu_{MS} \right]^2}$$
 (9)

The results in Fig. 9 can be explained as follows. The MRV portion of the pulse sequence encodes for particle velocity during the flow encoding gradients at the start of the pulse sequence, while the MRI portion of the pulse sequence encodes for particle positions during the imaging gradients, mainly when the imaging gradients pass through the center of k-space. Particle positions and velocities change as bubbles rise through the system during the 55 ms duration of the pulse sequence since the time for bubble pinch off, rise and eruption is roughly 144 ms as seen in Fig. 7. As such, simply averaging the positions and velocities over the entire 55 ms (Fig. 9a) is not a fully accurate description of what the MRI pulse sequence is actually measuring, nor is taking the particle positions and velocities during the flow encoding (Figs. 9b and d) or the imaging (Fig. 9c) portion of the pulse sequence. As such, the results indicate that when variations in flow dynamics occur over the same time frame as the length of the pulse sequence, processing of CFD or DEM data must take this into account by assessing velocities during flow encoding and concentration or signal intensity when imaging is at the center of k-space (Fig. 9e). Further, the results emphasize that rapid MRV techniques can only be taken as an effectively instantaneous measurement of dynamics when the time scale for fluctuations in flow and concentration is long as compared to the time of the pulse sequence. This conclusion is supported by the fact that the match between MRV and instantaneous particle velocities is very close for steady flows with effectively infinite time scales for flow fluctuations. In contrast, when the flow is unsteady in the fluidized beds, the faster the flow fluctuations become with decreasing particle size, the larger the mismatch between MRV and instantaneous particle velocities become, as seen in Table 1 and Fig. 10. This relationship can be expressed with:

$$\frac{t_{\text{flow fluc}}}{t_{\text{pulse seq}}} = \frac{dz/V_{\text{flow fluc}}}{t_{\text{pulse seq}}} > 1 \tag{9}$$

The ratio $t_{\text{flow fluc}}/t_{\text{pulse seq}}$ quantifies the fluctuation of flow during the duration of the pulse sequence. A number much higher than one means that the flow varies slower than the pulse sequence captures it while a number smaller means that the flow changes within one duration. Since the particle velocities fluctuate rapidly in time and space in fluidized beds, we approximate the fluctuating particle velocity, $V_{\text{flow fluc}}$, as the particle velocities observed themselves, V_z . In this case, the fastest particle velocities are 1000 mm/s and a pixel is 3.1 mm long in flow direction (dz), which results in a value for $t_{\text{flow fluc}}$ of 31 ms. With a pulse sequence duration of 55 ms, the ratio is 0.56, and thus it is not accurate to assess the MRV measurement simulated by JEMRIS as an effective instantaneous measurement of flow dynamics. Based on this assessment, the faster velocities are in a heterogeneous multiphase flow, the less likely rapid MRV is to produce an accurate measurement of the instantaneous flow field. Note that for a steady flow as in Fig. 5, the

time scale for flow fluctuations is infinity and no accuracy reduction due to instantaneous dynamics is expected from different MRI pulse sequences. This is seen in **Table 1**, since all types of CFD-DEM post-processing match JEMRIS equally for the steady plug flow. Note that the two simple steady flows shown here only have one-dimensional flow in the direction out of the imaging plane. Steady flow cases with more complex flow profiles including non-zero flow components along the imaging plane are susceptible of imaging artifacts arising from particle location and velocity being registered when the particle is at different points in space and time, as seen here for the unsteady flows.

Table 1. Normalized mean-squared difference (Eq. 8) between MRI simulation results and different post-processing methods of CFD-DEM. The numbers after \pm indicate the standard deviation in the normalized mean-squared difference (Eq. 9)

	Method a	Method b	Method $oldsymbol{c}$	Method d	Method e
steady flow (plug flow)	0.250 ± 0.001	0.250 ± 0.001	0.250 ± 0.001	0.250 ± 0.001	0.250 ± 0.001
Gas-jet injected Fluidized bed (3 mm particles)	177 ± 24	70 ± 12	78 ± 10	61 ± 11	26 ± 14
Gas-jet injected Fluidized bed (1 mm particles)	307 ± 9	741 ± 16	585 ± 19	770 ± 19	168 ± 8

The same set of simulations are repeated for 1 mm particles, with all other simulation parameters kept the same. Since drag force from the gas flow pushes smaller particles around more easily, the particles move faster and the bubbles have more complex dynamics in the 1 mm particle case than in the 3 mm particle case. Results of the simulations and the difference plots are presented in Fig. 10. During the 55 ms of the pulse sequence, the shape and position of jets and bubbles changes a large amount (Fig. 11b), with significantly more change than during the same time frame for the 3 mm particles (Fig. 11a). Thus, depending on the post-processing technique for the CFD-DEM data (Fig. 10a-e) different regions are voided of data, corresponding to where bubbles are registered from the post-processing. Since MRV measures particle positions mainly when the imaging gradients are in the center of k-space, post-processing of CFD-DEM data which does the same (Fig. 10c and e) match the bubble positions most closely. However, since MRV measures particle velocities largely at the center of the flow encoding gradients, the post-processing of CFD-DEM data in Fig. 10e matches that from JEMRIS most closely as quantified by the normalized mean-squared difference. The ratio $t_{\text{flow fluc}}/t_{\text{pulse seq}}$ sequence is even lower for the 1 mm particles at 0.036 due to the higher particle velocities, indicating that the approximation of rapid MRV as an instantaneous measurement of velocity field is even worse. This lower ratio explains why **Table 1** shows that the normalized mean-squared differences for the 1 mm particles in **Fig. 10** are higher than those for the 3 mm particles in **Fig. 9**.

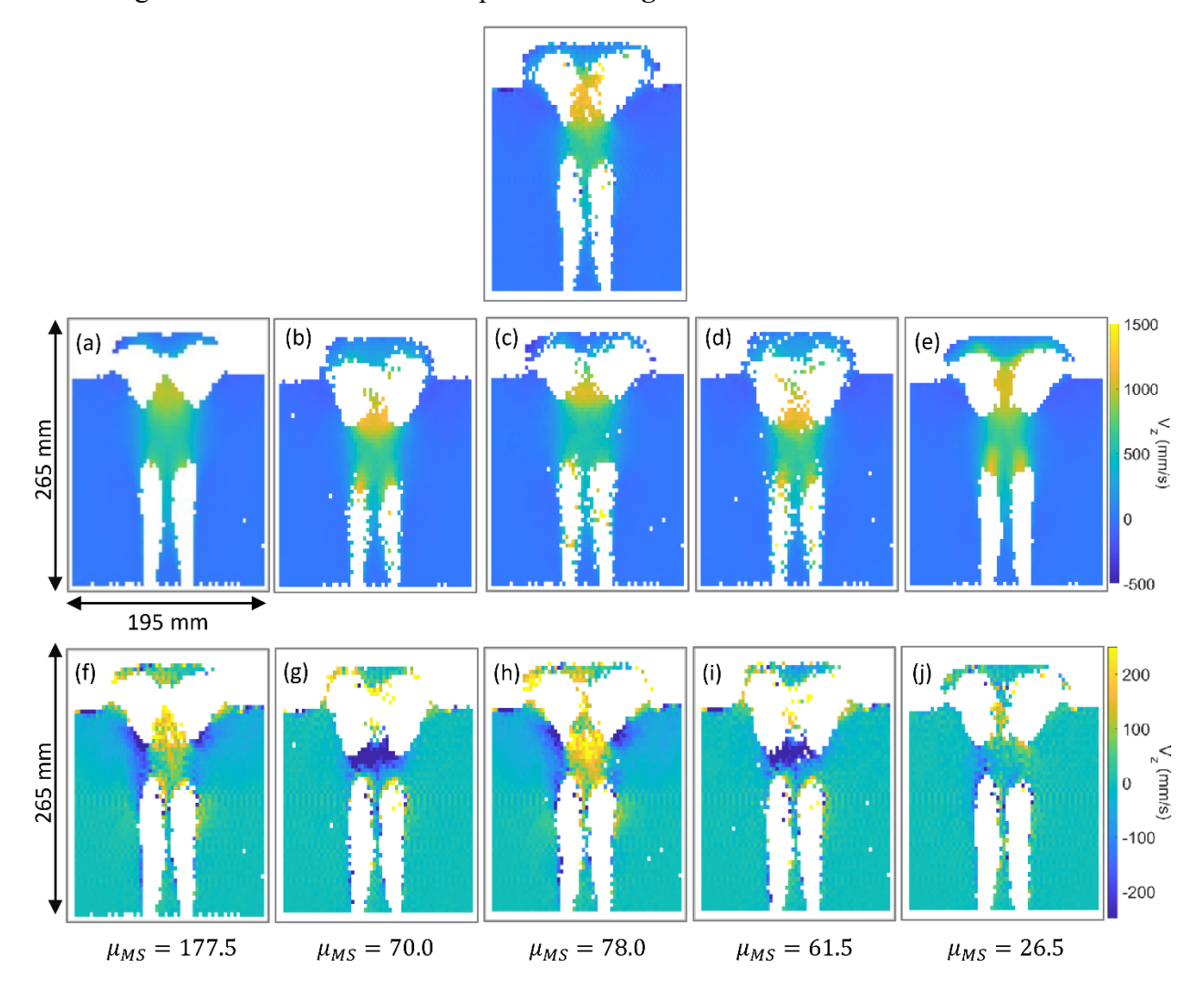


Fig. 9. Vertical velocity (V_z) obtained from JEMRIS (top row), CFD-DEM (a-e), and the corresponding difference plots (f-j), for 3 mm particles, and jet velocity of 40 m/s. (a and f) time-averaged velocity over the time frame of the entire pulse sequence, (b and g) time-averaged velocity over the time frame of the bipolar gradients, (c and h) instantaneous velocity at the time at which the imaging portion of the sequence is at the center of k-space, (d and i) instantaneous velocity at the time at the center of the bipolar gradients, (e and j) particle velocities taken at the instant in the center of the bipolar gradients, but particle positions taken later when the imaging gradients are in the center of k-space

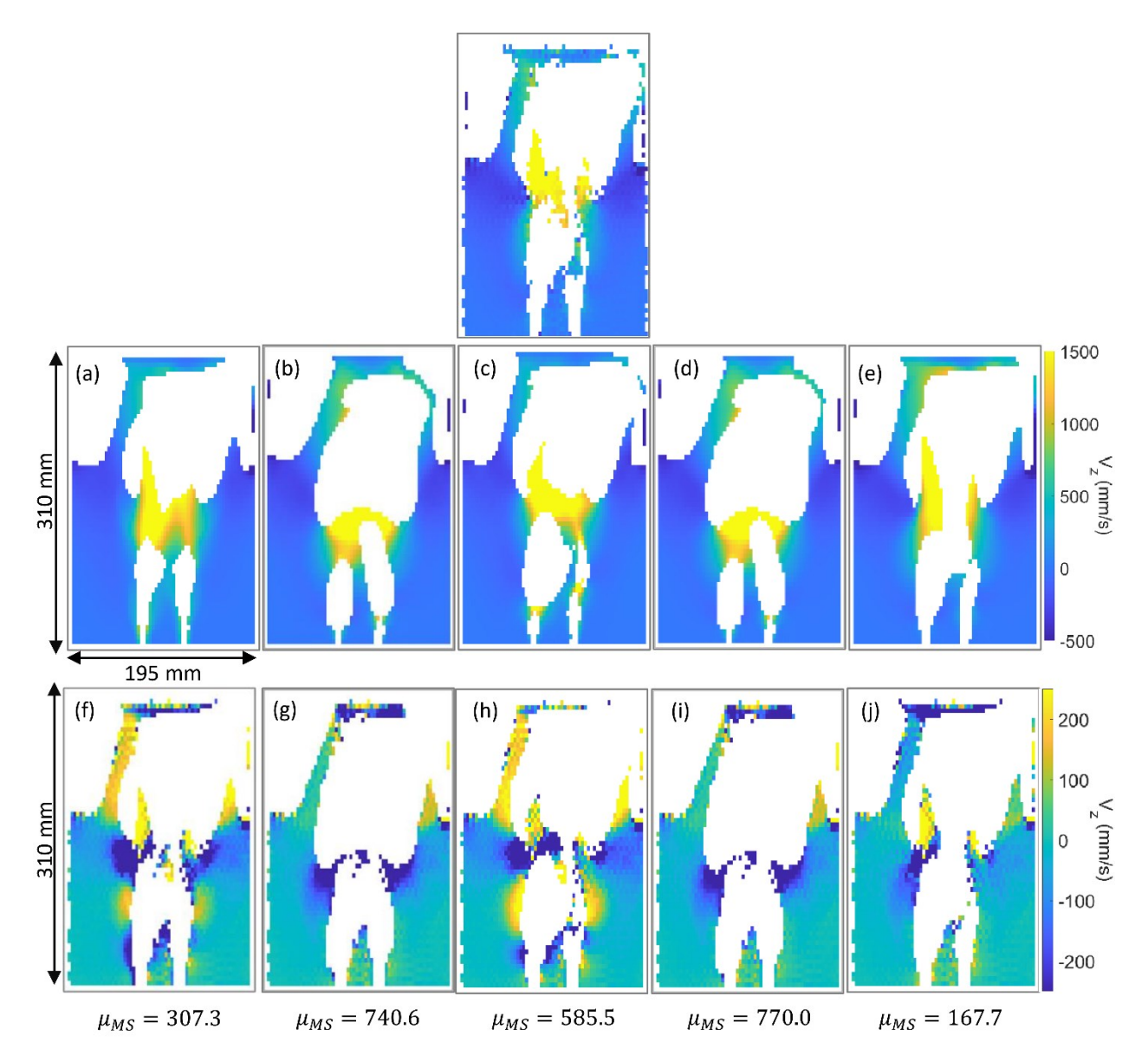


Fig. 10. Vertical velocity (V_z) obtained from JEMRIS (top row), CFD-DEM (a-e), and the corresponding difference plots (f-j), for 1 mm particles, and jet velocity of 40 m/s. (a and b) time-averaged velocity over the time frame of the entire pulse sequence, (c and d) time-averaged velocity over the time frame of the bipolar gradients, (e and f) instantaneous velocity at the time at which the imaging portion of the sequence is at the center of k-space, (i and j) instantaneous velocity at the time at the center of the bipolar gradients, (k and l) particle velocities taken at the instant in the center of the bipolar gradients, but particle positions taken later when the imaging gradients are in the center of k-space.

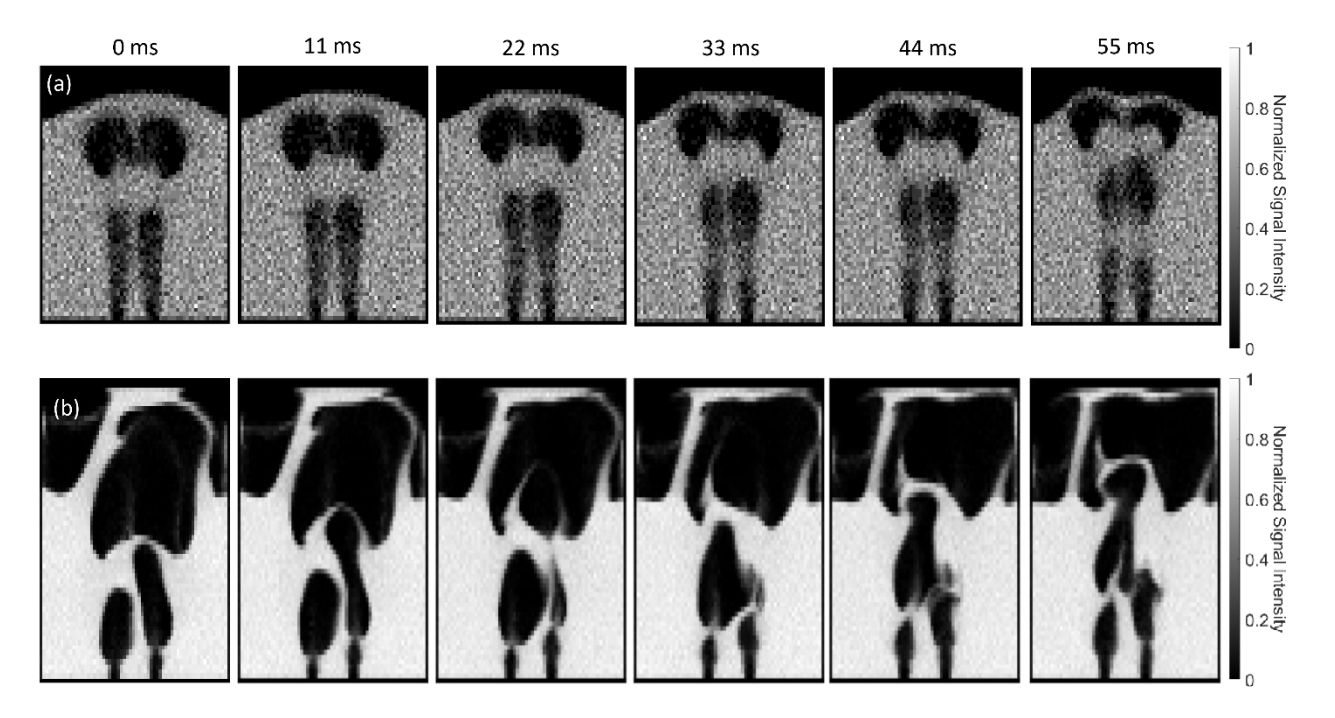


Fig. 11. Time-series images of signal intensity obtained from CFD-DEM post-processing on a central slice with a thickness of 10 mm for the case of (a) 3 mm particles, and (b) 1 mm particles. Signal intensity in MRI simulation is equivalent to average number of particles in each cell in CFD-DEM post-processing.

4 Conclusion

Rapid MRI and MRV offer some novel opportunities to non-invasively measure unsteady flow dynamics in opaque multiphase flow systems, and rapid MRI measurements have recently been used to assess the accuracy of flow simulations of fluidized beds ^{25,46}. The insights on flow physics gained from comparisons between MRI and flow simulations is limited by the potential artifacts in MRI measurements and the fact that identifying the best way to compare flow simulation data with MRI measurements is non-trivial. Here, we have first demonstrated through MRV simulation that an MRV measurement does not inherently introduce significant artifacts into velocity field, as seen by the comparison between CFD-DEM simulation and MRV simulation of steady flow. At the same time, the nature of MRV measurements makes it such that comparing an MRV measurement of an unsteady flow with flow simulation data from a single instant or averaged over the duration of the pulse sequence does not provide a fair assessment of the accuracy of the flow simulation if velocity fluctuations are much faster than the pulse sequence. Instead, the most accurate comparison of MRV measurements with CFD simulations comes from processing velocity data from the CFD data at a time corresponding to the center of the flow encoding gradients while taking position data at a later time corresponding to the center of k-space. This insight also highlights that rapid MRV measurements can only be approximated as instantaneous measurements of a flow field if the flow field is evolving much slower than the measurement duration. More rapid flow fluctuations in a multiphase flow make it more difficult to compare rapid MRV measurements with flow simulations.

Future work can expand upon this study in a number of ways. First, other pulse sequences, sources of noise and post-processing techniques can be incorporated to capture the physics of more advanced MRI techniques, such as partial Fourier scanning ⁴⁷ and SENSE reconstruction ⁴⁸. These developments to the MRI simulations would allow for higher temporal resolution while also incorporating new sources of artifacts in MRI measurements. Further, the k-space signal produced by a single spherical or ellipsoidal particle (as demonstrated in ⁴⁹) could be calculated and integrated into the MRI simulation framework presented here. Utilizing the Fourier shift theorem, the signal generated by moving particles could be modeled by incorporating this shape factor into the simulation of moving points presented here. This approach has the potential to increase the accuracy of k-space simulation and therefore improve the accuracy of the MRI simulations. Additionally, a recent work by Clarke et al. 50, has shown that rotation motion of particles can lead to substantial signal attenuation and hence to an amplified velocity variance. In the present work we did not take into account the effect of rotational motion on the MRI measurements. In future works, this effect could be incorporated into the simulation framework to increase its accuracy further. Further, the effect of slice-selecting gradients on flow measurement could be quantified in future studies as well as how these artifacts can be reduced by changing the shape of the sliceselecting gradients. Finally, flow and MRI simulations could be compared across a wider range of flow systems to view the effects studied here on MRI and CFD studies of e.g. dense suspensions, polymer solutions and hopper flows. As such, the framework provided by this paper can enable further insights into how to improve MRI measurements, flow simulations and the insights drawn from comparing MRI and CFD.

5 Acknowledgements

We acknowledge the National Science Foundation (NSF Grant #2144763 and #2024346), the Office of Naval Research (ONR Grant N00014-23-1-2041), as well as the German Research Foundation (DFG - Project number 471615686) for supporting this research.

6 References

- (1) Wiese, M.; Benders, S.; Blümich, B.; Wessling, M. 3D MRI Velocimetry of Non-Transparent 3D-Printed Staggered Herringbone Mixers. *Chem. Eng. J.* **2018**, *343*, 54–60.
- (2) Lovreglio, P.; Das, S.; Buist, K. A.; Peters, E.; Pel, L.; Kuipers, J. A. M. Experimental and Numerical Investigation of Structure and Hydrodynamics in Packed Beds of Spherical Particles. *AIChE J.* **2018**, *64* (5), 1896–1907.
- (3) Markl, M.; Schnell, S.; Wu, C.; Bollache, E.; Jarvis, K.; Barker, A. J.; Robinson, J. D.; Rigsby, C. K. Advanced Flow MRI: Emerging Techniques and Applications. *Clin. Radiol.* **2016**, *71* (8), 779–795.
- (4) Gladden, L. F.; Sederman, A. J. Recent Advances in Flow MRI. *J. Magn. Reson.* **2013**, 229, 2–11.
- (5) Xanthis, C. G.; Venetis, I. E.; Chalkias, A. V; Aletras, A. H. MRISIMUL: A GPU-Based Parallel Approach to MRI Simulations. *IEEE Trans. Med. Imaging* **2013**, *33* (3), 607–617.
- (6) Fortin, A.; Salmon, S.; Baruthio, J.; Delbany, M.; Durand, E. Flow MRI Simulation in

- Complex 3D Geometries: Application to the Cerebral Venous Network. *Magn. Reson. Med.* **2018**, *80* (4), 1655–1665.
- (7) Hazra, A.; Lube, G.; Raumer, H.-G. Numerical Simulation of Bloch Equations for Dynamic Magnetic Resonance Imaging. *Appl. Numer. Math.* **2018**, *123*, 241–255.
- (8) Shkarin, P.; Spencer, R. G. S. Direct Simulation of Spin Echoes by Summation of Isochromats. *Concepts Magn. Reson.* **1996**, *8* (4), 253–268.
- (9) Jochimsen, T. H.; Schäfer, A.; Bammer, R.; Moseley, M. E. Efficient Simulation of Magnetic Resonance Imaging with Bloch–Torrey Equations Using Intra-Voxel Magnetization Gradients. *J. Magn. Reson.* **2006**, *180* (1), 29–38.
- (10) Brenner, A. R.; Kürsch, J.; Noll, T. G. Distributed Large-Scale Simulation of Magnetic Resonance Imaging. *Magn. Reson. Mater. Physics, Biol. Med.* **1997**, *5*, 129–138.
- (11) Kose, R.; Kose, K.; Terada, Y.; Tamada, D.; Motosugi, U. Development of a Method for the Bloch Image Simulation of Biological Tissues. *Magn. Reson. Imaging* **2020**, *74*, 250–257.
- (12) Stöcker, T.; Vahedipour, K.; Shah, N. J. Simulation of Spin Dynamics: A Tool in MRI System Development. In *Journal of Physics: Conference Series*; IOP Publishing, 2011; Vol. 295, p 12020.
- (13) Majka, P.; Wójcik, D. K. Possum—a Framework for Three-Dimensional Reconstruction of Brain Images from Serial Sections. *Neuroinformatics* **2016**, *14*, 265–278.
- (14) Mohammadi-Nejad, A. R.; Hossein-Zadeh, G.-A. Simulation of Echo Planar Imaging in MRI: Application to Assessment of Field Inhomogeneity and Chemical Shift. In 2007 9th International Symposium on Signal Processing and Its Applications; IEEE, 2007; pp 1–4.
- (15) Ravi, K. S.; Potdar, S.; Poojar, P.; Reddy, A. K.; Kroboth, S.; Nielsen, J.-F.; Zaitsev, M.; Venkatesan, R.; Geethanath, S. Pulseq-Graphical Programming Interface: Open Source Visual Environment for Prototyping Pulse Sequences and Integrated Magnetic Resonance Imaging Algorithm Development. *Magn. Reson. Imaging* **2018**, *52*, 9–15.
- (16) Stöcker, T.; Vahedipour, K.; Pflugfelder, D.; Shah, N. J. High-performance Computing MRI Simulations. *Magn. Reson. Med.* **2010**, *64* (1), 186–193.
- (17) Jurczuk, K.; Kretowski, M.; Eliat, P.-A.; Bellanger, J.-J.; Saint-Jalmes, H.; Bézy-Wendling, J. A New Approach in Combined Modeling of MRI and Blood Flow: A Preliminary Study. In 2012 9th IEEE International Symposium on Biomedical Imaging (ISBI); IEEE, 2012; pp 812–815.
- (18) Jurczuk, K.; Kretowski, M.; Eliat, P.-A.; Saint-Jalmes, H.; Bezy-Wendling, J. In Silico Modeling of Magnetic Resonance Flow Imaging in Complex Vascular Networks. *IEEE Trans. Med. Imaging* **2014**, *33* (11), 2191–2209.
- (19) Fortin, A.; Durand, E.; Salmon, S. Extension of an Mri Simulator Software for Phase Contrast Angiography Experiments. In *International Symposium on Biomedical Simulation*; Springer, 2014; pp 150–154.
- (20) Boyce, C. M.; Holland, D. J.; Scott, S. A.; Dennis, J. S. Adapting Data Processing to Compare Model and Experiment Accurately: A Discrete Element Model and Magnetic

- Resonance Measurements of a 3d Cylindrical Fluidized Bed. *Ind. Eng. Chem. Res.* **2013**, 52 (50), 18085–18094.
- (21) Boyce, C. M.; Rice, N. P.; Ozel, A.; Davidson, J. F.; Sederman, A. J.; Gladden, L. F.; Sundaresan, S.; Dennis, J. S.; Holland, D. J. Magnetic Resonance Characterization of Coupled Gas and Particle Dynamics in a Bubbling Fluidized Bed. *Phys. Rev. Fluids* **2016**, *1* (7), 74201.
- (22) Boyce, C. M.; Penn, A.; Lehnert, M.; Pruessmann, K. P.; Müller, C. R. Magnetic Resonance Imaging of Single Bubbles Injected into Incipiently Fluidized Beds. *Chem. Eng. Sci.* **2019**, *200*, 147–166.
- (23) Boyce, C. M.; Penn, A.; Lehnert, M.; Pruessmann, K. P.; Müller, C. R. Effect of Liquid Bridging on Bubbles Injected into a Fluidized Bed: A Magnetic Resonance Imaging Study. *Powder Technol.* **2019**, *343*, 813–820.
- (24) Penn, A.; Tsuji, T.; Brunner, D. O.; Boyce, C. M.; Pruessmann, K. P.; Müller, C. R. Real-Time Probing of Granular Dynamics with Magnetic Resonance. *Sci. Adv.* **2017**, *3* (9), e1701879.
- (25) Xi, K.; Guo, Q.; Boyce, C. M. Comparison of CFD-DEM and TFM Simulations of Single Bubble Injection in 3D Gas-Fluidized Beds with MRI Results. *Chem. Eng. Sci.* **2021**, *243*, 116738.
- (26) Boyce, C. M.; Ozel, A.; Rice, N. P.; Rubinstein, G. J.; Holland, D. J.; Sundaresan, S. Effective Particle Diameters for Simulating Fluidization of Non-spherical Particles: CFD-DEM Models vs. MRI Measurements. *AIChE J.* **2017**, *63* (7), 2555–2568.
- (27) Clarke, D. A.; Sederman, A. J.; Gladden, L. F.; Holland, D. J. Investigation of Void Fraction Schemes for Use with CFD-DEM Simulations of Fluidized Beds. *Ind. Eng. Chem. Res.* **2018**, *57* (8), 3002–3013.
- (28) Seymour, J. D.; Caprihan, A.; Altobelli, S. A.; Fukushima, E. Pulsed Gradient Spin Echo Nuclear Magnetic Resonance Imaging of Diffusion in Granular Flow. *Phys. Rev. Lett.* 2000, 84 (2), 266.
- (29) Ehrichs, E. E.; Jaeger, H. M.; Karczmar, G. S.; Knight, J. B.; Kuperman, V. Y.; Nagel, S. R. Granular Convection Observed by Magnetic Resonance Imaging. *Science* (80-.). 1995, 267 (5204), 1632–1634.
- (30) Werther, J. Fluidized-bed Reactors. *Ullmann's Encycl. Ind. Chem.* **2000**.
- (31) Khan, M. J. H.; Hussain, M. A.; Mansourpour, Z.; Mostoufi, N.; Ghasem, N. M.; Abdullah, E. C. CFD Simulation of Fluidized Bed Reactors for Polyolefin Production—A Review. *J. Ind. Eng. Chem.* **2014**, *20* (6), 3919–3946.
- (32) Sansare, S.; Aziz, H.; Sen, K.; Patel, S.; Chaudhuri, B. Computational Modeling of Fluidized Beds with a Focus on Pharmaceutical Applications: A Review. *J. Pharm. Sci.* **2022**, *111* (4), 1110–1125.
- (33) Padash, A.; Boyce, C. CFD-DEM Study of Anomalous Collapse of Interacting Bubbles into an Incipiently Fluidized Bed. *Bull. Am. Phys. Soc.* **2020**, *65*.
- (34) Cundall, P. A.; Strack, O. D. L. A Discrete Numerical Model for Granular Assemblies.

- geotechnique 1979, 29 (1), 47-65.
- (35) Norouzi, H. R.; Zarghami, R.; Sotudeh-Gharebagh, R.; Mostoufi, N. *Coupled CFD-DEM Modeling: Formulation, Implementation and Application to Multiphase Flows*; John Wiley & Sons, 2016. https://doi.org/10.1002/9781119005315.
- (36) JEMRIS. https://www.jemris.org/ (accessed 2022-08-19).
- (37) *Introduction*. https://www.jemris.org/ug intro.html (accessed 2021-11-03).
- (38) Bloch, F. Nuclear Induction. *Phys. Rev.* **1946**, 70 (7–8), 460.
- (39) Stöcker, T. Realistic Simulation of Parallel Transmission in MRI. In 2019 International Conference on Electromagnetics in Advanced Applications (ICEAA); IEEE, 2019; pp 864–867.
- (40) Ancel, A.; Fortin, A.; Garnotel, S.; Miraucourt, O.; Tarabay, R. PHANTOM Project: Development and Validation of the Pipeline from MRA Acquisition to MRA Simulations. *ESAIM Proc. Surv.* **2016**, *55*, 1–22.
- (41) Marshall, I. Simulation of In-plane Flow Imaging. *Concepts Magn. Reson.* **1999**, *11* (6), 379–392.
- (42) Mensing, D. Towards Automated Quality Assessment with Deep Learning: Classification, Quantification and Correction of MRI Artefacts, Universität Bremen, 2020.
- (43) Smith, T. B. MRI Artifacts and Correction Strategies. *Imaging Med.* **2010**, *2* (4), 445.
- (44) Penn, A.; Padash, A.; Lehnert, M.; Pruessmann, K. P.; Müller, C. R.; Boyce, C. M. Asynchronous Bubble Pinch-off Pattern Arising in Fluidized Beds Due to Jet Interaction: A Magnetic Resonance Imaging and Computational Modeling Study. *Phys. Rev. fluids* **2020**, *5* (9), 94303.
- (45) Penn, A.; Boyce, C. M.; Prüssmann, K. P.; Müller, C. R. Regimes of Jetting and Bubbling in a Fluidized Bed Studied Using Real-Time Magnetic Resonance Imaging. *Chem. Eng. J.* **2020**, *383*, 123185.
- (46) Xi, K.; Kovar, T.; Fullmer, W. D.; Penn, A.; Musser, J.; Boyce, C. M. CFD-DEM Study of Bubble Properties in a Cylindrical Fluidized Bed of Geldart Group D Particles and Comparison with Prior MRI Data. *Powder Technol.* **2021**, *389*, 75–84.
- (47) McGibney, G.; Smith, M. R.; Nichols, S. T.; Crawley, A. Quantitative Evaluation of Several Partial Fourier Reconstruction Algorithms Used in MRI. *Magn. Reson. Med.* **1993**, *30* (1), 51–59.
- (48) Pruessmann, K. P.; Weiger, M.; Scheidegger, M. B.; Boesiger, P. SENSE: Sensitivity Encoding for Fast MRI. *Magn. Reson. Med. An Off. J. Int. Soc. Magn. Reson. Med.* **1999**, 42 (5), 952–962.
- (49) Koay, C. G.; Sarlls, J. E.; Özarslan, E. Three-dimensional Analytical Magnetic Resonance Imaging Phantom in the Fourier Domain. *Magn. Reson. Med. An Off. J. Int. Soc. Magn. Reson. Med.* **2007**, *58* (2), 430–436.
- (50) Clarke, D. A.; Fabich, H. T.; Brox, T. I.; Galvosas, P.; Holland, D. J. On the Influence of Rotational Motion on MRI Velocimetry of Granular Flows—Theoretical Predictions and Comparison to Experimental Data. J. Magn. Reson. 2019, 307, 106569.

Table of Contents Figure:

